J. Fluid Mech. (2002), *vol.* 470, *pp.* 115–133.
DOI: 10.1017/S0022112002002008 Printed in the United Kingdom

Zonal flow driven by strongly supercritical convection in rotating spherical shells

By U. R. CHRISTENSEN

Institut für Geophysik, Herzberger Landstrasse 180, 37075 Göttingen, Germany

(Received 22 October 2001 and in revised form 13 June 2002)

Thermal convection in a rotating spherical shell with free-slip boundaries can excite a dominant mean zonal flow in the form of differentially rotating cylinders concentric to the principal rotation axis. This process is studied numerically for Prandtl numbers of order 1, Ekman numbers in the range $E = 3 \times 10^{-4}$–10^{-5}, and Rayleigh numbers up to 100× critical. Small-scale convection transfers kinetic energy into the mean zonal flow via Reynolds stresses. For low Ekman number and high Rayleigh number, the force balance is predominantly among the Coriolis, inertial and buoyancy forces, and viscosity plays a minor role. A modified Rayleigh number Ra^* is introduced, which does not depend on viscosity or thermal diffusivity, and asymptotic scaling laws for the dependence of various properties on Ra^* in the limit of negligible viscosity ($E \to 0$) are estimated from the numerical results. The ratio of kinetic energy in the zonal flow to that in the non-zonal (convective) flow increases strongly with Ra^* at low supercritical Rayleigh number, but drops at high values of Ra^*. This is probably caused by the gradual loss of geostrophy of the convective columns and a corresponding decorrelation of Reynolds stresses. Applying the scaling laws to convection in the molecular hydrogen envelopes of the large gas planets predicts the observed magnitude of the zonal winds at their surfaces.

1. Introduction

Thermal convection in thick rotating spherical shells (as opposed to thin shells such as planetary atmospheres or ocean layers) plays a role in various cosmic objects, for example the Earth's liquid core, stars, the large fluid planets of the solar system and perhaps the newly discovered Jupiter-sized extrasolar planets. Linear theory (Roberts 1968; Busse 1970; Jones, Soward & Mussa 2000) predicts that at small Ekman number $E = \nu/\Omega D^2$, where ν is viscosity, Ω rotation frequency and D the shell thickness, the flow at the onset of convection is organized in nearly geostrophic columns whose width scales as $E^{1/3}$. This has been confirmed in experimental (Busse & Carrigan 1976) and numerical studies (Zhang 1992). Of particular interest is the excitation of a strong mean zonal flow, or differential rotation, such as is found in the Sun, at the surface of the large gas planets, and perhaps in the Earth's core. In an electrically conducting fluid, differential rotation can play an important role in the generation of toroidal magnetic field; however, the electromagnetic forces will also tend to break differential motions. In the insulating molecular hydrogen layers of Jupiter and Saturn, where electromagnetic coupling plays no role, the zonal flow can become very strong in relation to the velocity of convection. At the surface of Jupiter the mean zonal flow is approximately five times stronger than the non-zonal (eddy) component (Ingersoll *et al.* 1981). Busse (1983) suggested that the internal convection transfers

kinetic energy into differential rotation of geostrophic cylinders that extend through the planetary interior. The latitudinal flow bands would be the surface expressions of these cylinders. However, this interpretation remained contested (e.g. Williams 1985).

Columnar convection can drive a large-scale zonal flow through Reynolds stresses, which arise from the inertial term $\boldsymbol{u} \cdot \nabla \boldsymbol{u}$ in the Navier–Stokes equation when the u_ϕ- (azimuthal) and the u_s- (cylindrically radial) velocity components are correlated. The curvature of the outer shell boundary, on which the convection columns impinge, causes a tilt of the columns, which implies a correlation of the two flow components (Busse 1983, 1994). Because the zonal flow is driven through the nonlinear term in the Navier–Stokes equation, its amplitude relative the convective flow velocity can only be predicted by finite-amplitude calculations. Zhang (1992) showed in numerical calculations that the zonal velocity can dominate the convective velocity even at rather weakly supercritical Rayleigh numbers when the Prandtl number is small. Sun, Schubert & Glatzmaier (1993) reported differential rotation in multiple cylinders for a strongly supercritical Rayleigh number, but found the zonal velocity to be an order of magnitude weaker than the convective velocity. However, their calculation did not get beyond the initial spin-up stage (Christensen 2001) and the result is not representative of an equilibrated state. A systematic exploration of the pattern and properties of convection at Rayleigh numbers up to ten times critical has been performed by Ardes, Busse & Wicht (1997) and Tilgner & Busse (1997) at an Ekman number of the order 10^{-3}. More recent numerical calculations at Ekman numbers around 10^{-4} confirmed the dominance of zonal flow at Rayleigh numbers a few times supercritical (Grote, Busse & Tilgner 2000; Aurnou & Olson 2001; Christensen 2001; Grote & Busse 2001). The zonal flow is prograde at low latitude near the outer boundary and retrograde near the tangent cylinder that encloses the central core. At a Prandtl number of 1 three different regimes have been identified depending on the Rayleigh number. Up to two or three times the critical value, convection is stationary aside from a longitudial drift of the pattern and the zonal velocity is less than or equal to the convective velocity. At Rayleigh numbers about ten times supercritical the zonal flow dominates by a factor that depends on the Ekman number and convection is strongly oscillatory (Grote *et al.* 2000). At even higher Rayleigh number convection is vigorous at all times and fills the entire volume (Christensen 2001).

Free-slip boundaries are a requirement for dominant zonal flow, at least in the parameter range covered by the numerical simulations. With rigid boundaries, the zonal flow has a similar pattern, but contributes only 10–20% to the total kinetic energy (Aurnou & Olson 2001). In laboratory experiments with rotating spheres lower Ekman numbers can be achieved than in current numerical models. Sumita & Olson (2000) observed significant zonal flow in experiments at high supercritical Rayleigh number. Aubert *et al.* (2001) showed in experiments with liquid gallium that at very low Prandtl number the zonal flow dominates even in a container with rigid walls.

Compared to geophysical or astrophysical applications, the numerical simulations and to a lesser extent the laboratory experiments are performed at much more moderate parameter values, in particular at Ekman numbers that are many orders of magnitude larger than the planetary values. Hence viscosity (and thermal diffusivity) plays a larger role and the dynamic flow regimes may differ. Aubert *et al.* (2001) present a scaling analysis suggesting that in their gallium experiments viscosity is negligible for the convective flow and convection is controlled by a balance between Coriolis force, inertia and buoyancy.

The present paper extends the numerical analysis by Christensen (2001) and concentrates on fully developed convection at Rayleigh numbers up to 100× critical

at the lowest practical values of the Ekman number $E \geqslant 10^{-5}$. The main purpose is to find asymptotic relations for the limit where viscosity plays a negligible role.

2. Equations and numerical method

Thermal convection of a Boussinesq fluid of constant material properties in a spherical shell rotating with the mean frequency Ω about the z-direction is considered. Gravity is assumed to vary linearly between the inner radius r_i and outer radius r_o. The ratio $\eta = r_i/r_o$ is set to 0.35. The boundaries are isothermal with an imposed temperature contrast of ΔT and the free-slip condition is used.

With the shell thickness $D = r_o - r_i$ as length scale, ΔT as temperature scale and Ω^{-1} as time scale, the dimensionless equations for the velocity $\boldsymbol{u}$, temperature T and non-hydrostatic pressure P are

$$\frac{\partial \boldsymbol{u}}{\partial t} + \boldsymbol{u}\cdot\nabla\boldsymbol{u} + 2\hat{\boldsymbol{z}}\times\boldsymbol{u} + \nabla P = E\nabla^2\boldsymbol{u} + Ra^*\boldsymbol{r}/r_o T, \tag{2.1}$$

$$\nabla\cdot\boldsymbol{u} = 0, \tag{2.2}$$

$$\frac{\partial T}{\partial t} + \boldsymbol{u}\cdot\nabla T = EPr^{-1}\nabla^2 T. \tag{2.3}$$

$Pr = \nu/\kappa$ is the Prandtl number, with κ the thermal diffusivity. We note that with the chosen scaling the dimensionless velocity is equivalent to a local Rossby number. In most calculations Pr is set to 1, but in § 3.5 the influence of varying Pr is addressed. Conventionally, time is scaled by the thermal or viscous diffusion time in convection problems. Because here time is scaled by the rotation period, a modified Rayleigh number appears in the equations:

$$Ra^* = \frac{\alpha g_o \Delta T}{\Omega^2 D}, \tag{2.4}$$

where α is thermal expansivity and g_o gravity at the outer radius r_o. The relation to the usual form of Rayleigh number

$$Ra = \frac{\alpha g_o \Delta T D^3}{\kappa\nu}, \tag{2.5}$$

is given by

$$Ra^* = RaE^2Pr^{-1}. \tag{2.6}$$

The main advantage of the modified form of the Rayleigh number is that it depends neither on viscosity nor on the thermal diffusivity. In a regime where viscosity does not play an important role in the force balance, the properties of the flow should be a function of Ra^* rather than of Ra. It is also useful to introduce a modified Rayleigh number based on the heat flux instead of the temperature contrast:

$$Ra_q^* = \frac{\eta\alpha g_o q}{\rho c \Omega^3 D^2} = Ra^* Nu^* = RaNuE^3Pr^{-2}. \tag{2.7}$$

Here q is the heat flux per unit area on the outer boundary, ρ the density, c the specific heat capacity. Nu^* is a modified Nusselt number as a measure of radial heat transport:

$$Nu^* = NuEPr^{-1} = \frac{\eta q}{\rho c \Delta T \Omega D}, \tag{2.8}$$

where

$$Nu = \eta q D/(\rho c \kappa \Delta T) \tag{2.9}$$

is the usual Nusselt number; the geometry factor η ensures that $Nu = 1$ in the conductive state. The advantage of the modified Nusselt number is again the independence from the diffusion parameter. The flux-based Rayleigh number Ra_q^* is, for fixed temperature boundary conditions, not a control parameter and must be calculated *a posteriori*. However, for an application to geophysical and astrophysical problems, it is useful to express results in terms of Ra_q^*, because fair estimates for the heat flux are usually available whereas the driving (superadiabatic) temperature contrast is poorly known.

In order to solve equations (2.1)–(2.3), the velocity is represented by poloidal (W) and toroidal (Z) scalar potentials:

$$\boldsymbol{u} = \nabla \times \nabla \times W\hat{\boldsymbol{r}} + \nabla \times Z\hat{\boldsymbol{r}}. \tag{2.10}$$

W, Z, P and T are expanded in Chebychev polynomials up to degree N_c in the radial direction and in spherical harmonic functions up to degree and order ℓ_{max} in the angular (θ, ϕ) coordinates. Equations for W and P combined are obtained from the radial component and from the horizontal divergence of (2.1); the equation for Z is obtained from the radial component of the curl of equation (2.1). The Chebychev coefficients are calculated separately for each harmonic mode (ℓ, m) by a collocation method on N_r radial grid points given by $r_k = (r_i + r_o + \cos(k\pi/N_r))/2$. Terms resulting from diffusion, ∇P, and the explicit time derivatives decouple in (ℓ, m) and are treated implicitly. Nonlinear terms and the Coriolis term are treated explicity by calculating them on a grid in (r, θ, ϕ) and projecting the result on the different harmonic modes (spectral transform method). To reduce aliasing effects, the number of latitudinal (N_θ) and longitudinal (N_ϕ) grid points is larger than ℓ_{max} or $2\ell_{max}$, respectively; likewise $N_r > N_c$. Complete de-aliasing would be achieved when the number of grid points is 1.5 times the number of modes, but an intermediate factor was found to be sufficient in the present models. The solution is advanced in time by a second-order Adams–Bashforth scheme and the time step is limited to a fraction of the Courant step. A more detailed description of the method is given in Glatzmaier (1984) or Tilgner (1999).

At the highest Ekman number convection is modelled for the full sphere without symmetry assumptions. For $E \leqslant 10^{-4}$ twofold symmetry in longitude is assumed ($m_s = 2$) or fourfold symmetry ($m_s = 4$) in the most demanding calculations. This retains only terms of even order m or multiples of four, respectively, in the harmonic expansion. Because convection at low Ekman number is dominated by high azimuthal wavenumbers, this is not considered to be a serious restriction. At low supercritical Rayleigh numbers each calculation was started from a conductive thermal state with superimposed noise. At high Ra a solution at different parameter values was taken as starting point.

The kinetic energy density is

$$E_k = \frac{1}{V_s E^2} \int u^2 \, \mathrm{d}V, \tag{2.11}$$

where V_s is the shell volume. Taking the integral (2.11) only over the poloidal components of the velocity field, the axisymmetric toroidal component, or the harmonic terms with $m > 0$, gives the poloidal energy E^{pol}, the zonal wind energy $E_{tor}^{m=0}$, or the non-zonal energy E^{nz}, respectively. The time evolution of energy components and of

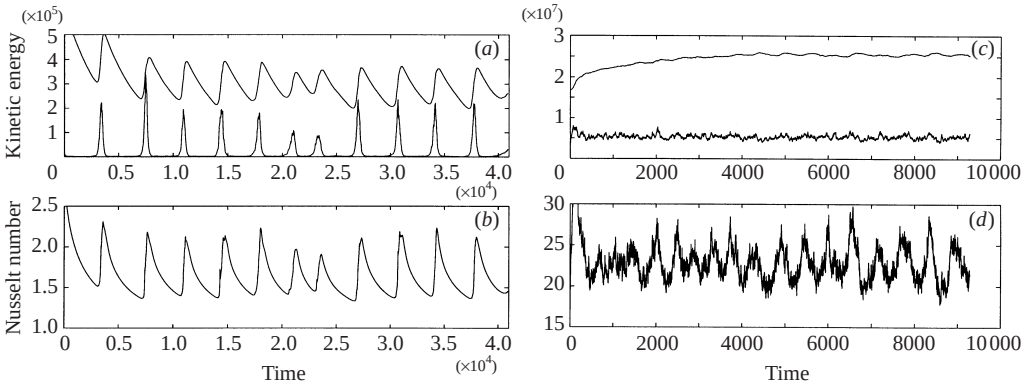

FIGURE 1. Time series for convection at $E = 10^{-5}$, $Pr = 1$, and a Rayleigh number 11.9× supercritical in (a, b) and 105× supercritical in (c, d). The upper lines in (a) and (c) are the zonal wind energies while the lower lines are the poloidal energies multiplied by a factor of 10. (b) and (d) show the Nusselt numbers.

E	Pr	Ra^*_{crit}	m_{crit}
3×10^{-4}	1	0.016790	6
1×10^{-4}	1	0.006510	8
3×10^{-5}	1	0.002413	12
1×10^{-5}	1	0.001005	16
1×10^{-5} (rigid)	1	0.001057	15
1×10^{-4}	0.3	0.012120	7
1×10^{-4}	3	0.003078	8

TABLE 1. Critical Rayleigh number and azimuthal wavenumber.

the Nusselt number have been monitored in each case to ensure that the solution is integrated past the transient stage. Two examples are shown in figure 1. Representative mean values of various properties are calculated by averaging only the final part of each time series where no appreciable drift is found. The question of the time required for the solution to equilibrate is further discussed in § 3.2.

3. Results

Critical values of the Rayleigh number Ra^*_{crit} and the critical azimuthal wavenumber m_{crit} have been calculated by monitoring the growth or decay of small perturbations of the conductive temperature profile. The results with an estimated accuracy of better than 1% are listed in table 1.

The variation of Ra^*_{crit} with the Ekman number is slightly stronger in this range than the asymptotic dependence with $E^{2/3}$, equivalent to the variation of Ra_{crit} with $E^{-4/3}$ (Busse 1970), but seems to approach the predicted exponent at lower E.

3.1. *Flow regimes at* $Pr = 1$

Figures 2 and 3 illustrate some characteristic pattern of convection at an Ekman number of 10^{-5} for weakly and strongly supercritical Rayleigh number, respectively. At low Rayleigh number, the convection pattern is stationary in a drifting frame of reference. Convection occurs only outside the inner-core tangent cylinder but is

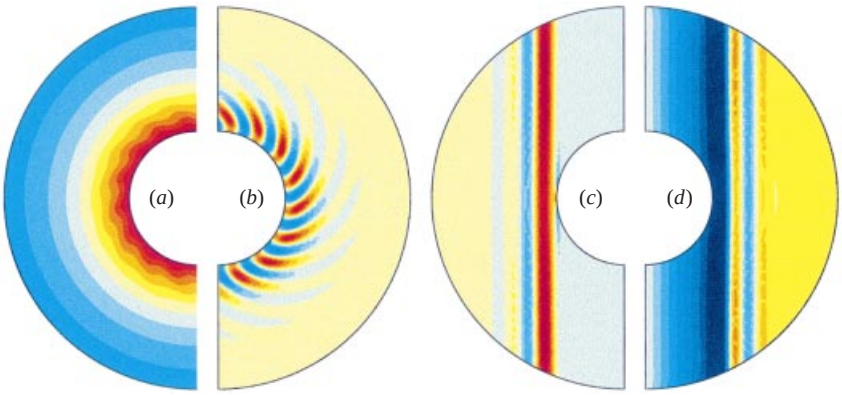

FIGURE 2. Quasi-stationary convection at $Ra^* = 0.0015$, $E = 10^{-5}$, $Pr = 1$. (*a*) Isotherms, (*b*) z-component of vorticity ω_z in the equatorial plane, (*c*) ω_z in a cut along the rotation axis, (*d*) azimuthal velocity in the same cut. Contour steps are 0.1 for T, 2.5×10^{-3} for ω_z and 3×10^{-5} for u_ϕ. Positive values of vorticity and velocity in yellow to red colours, negative in blue.

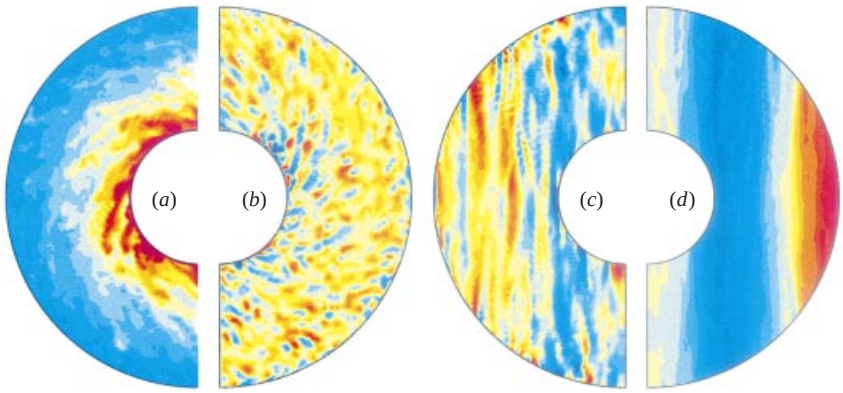

FIGURE 3. Chaotic convection at $Ra^* = 0.045$, $E = 10^{-5}$, $Pr = 1$. (*a*) Isotherms, (*b*) z-component of vorticity ω_z in the equatorial plane, (*c*) ω_z in a cut along the rotation axis, (*d*) azimuthal velocity in the same cut. Contour steps are 0.06 for T, 8×10^{-2} for ω_z and 8×10^{-3} for u_ϕ.

strongly concentrated near its boundary. In most of the volume of the spherical shell the fluid is nearly stagnant. In equatorial sections (figure 2*a*, *b*) a pinwheel pattern can be seen in the vorticity and temperature fields. Despite the fairly low Rayleigh number, the mean zonal flow carries 62% of the total kinetic energy. The flow is strongly geostrophic, i.e. nearly independent of the z-coordinate (figure 2*c*, *d*). At high Rayleigh number, convection is very chaotic and fills the entire space, including the region inside the tangent cylinder. The mean zonal flow dominates strongly and contains on time-average 97.6% of the kinetic energy in this case. Thermal plumes are strongly tilted in the prograde direction by the shear of the zonal flow (figure 3*a*). However, individual convective vortices in the equatorial plane are rather scattered and do not form convection cells that stretch over the entire radius (figure 3*b*). A preferred prograde tilt of the vortices is discernible, but is not strongly pronounced. The zonal flow in particular is still approximately geostrophic (figure 3*d*). Individual convective vortices are elongated along the rotation axis; however, some bend away from the z-direction, and they are often not continuous throughout the entire shell (figure 3*c*).

Time-averaged properties of the flow are listed in table 2 for all calculations with a Prandtl number of 1. The numerical resolution is also indicated. The Reynolds number based on the r.m.s.-velocity is $Re = \sqrt{2E_k}$ and the Reynolds number for the poloidal flow alone, Re^{pol}, is obtained accordingly with E^{pol}. The latter describes the vigour of the convective flow (without the zonal wind). While columnar convection comprises both poloidal and toroidal flow components of about equal strength, the poloidal part alone transports heat in the radial direction and is therefore characteristic of the convective flow *per se*. The respective Rossby numbers are obtained from $Ro = ERe$ and $Ro^{pol} = ERe^{pol}$.

For Rayleigh numbers larger than a few times critical, the flow becomes time dependent. At about 10 times supercritical the flow is strongly oscillatory (figure 1*a*, *b*). In particular, the vigour of the convective part changes drastically: periods of virtual quiescence are interrupted by short and intense bursts in a nearly periodic manner (Grote *et al.* 2000; Grote & Busse 2001; Christensen 2001). The convective bursts replenish the energy in the mean zonal flow, which decays by viscous friction between these events. During a burst, the convective flow fills the entire volume outside the tangent cylinder, whereas the weak residual convection between bursts is restricted to the vicinity of the tangent cylinder boundary. In order to quantify the degree of time dependence, the variance of the poloidal kinetic energy with time, Var^{pol}, normalized with its mean value, is listed in table 2. The relative variance becomes larger for lower Ekman numbers, and peaks at nearly 200% for $E = 10^{-5}$. However, while these strong oscillations are a remarkable phenomenon, they are restricted to intermediate Rayleigh numbers. At sufficiently supercritical Rayleigh number, convection is always vigorous and space-filling (figure 1*c*), and the relative variance in the poloidal kinetic energy becomes small. This is called the regime of fully developed convection. Also, very pronounced oscillations are found only for a Prandtl number of 1. Both at larger and smaller Prandtl number the oscillations are weaker and less regular.

3.2. *Validation of results*

The use of a restricted number of azimuthal modes and the rather limited run time of most simulations (a fraction of the viscous diffusion time D^2/ν at high Rayleigh number) may conceivably compromise the reliability of the results. Both are tested in this section.

Two selected simulations with imposed twofold longitudinal symmetry have been compared with full-sphere calculations at the same parameter values. For fully developed convection at $Ra^*/Ra^*_{crit} = 31$, $E = 10^{-4}$, the amplitude of time-dependent fluctuations in the global properties is slightly larger with imposed symmetry. However, the mean values, averaged over $t = 10^4$ (one diffusion time) agree within 1%. In the regime of strongly oscillatory convection at $E = 3 \times 10^{-5}$ and $Ra^*/Ra^*_{crit} = 22$, a calculation was started with twofold symmetry and continued until a characteristic oscillation pattern had been established. The run was then continued with the symmetry assumption relaxed. A weak thermal perturbation of order $m = 1$ was added to facilitate the excitation of odd-order modes. After a short time they contained the same power as the even-order modes (aside from $m = 0$). No fundamental differences before and after the change are found in the period and amplitude of the oscillations or in time-averaged properties (figure 4).

Several time scales must be considered for the evolution of the solutions. At low Rayleigh number it is expected that the solution equilibrates on a viscous time scale, more precisely on the scale of the slowest relevant viscous decay mode. The strongly oscillatory regime offers an opportunity to estimate this relaxation time, from the

Ra^*/Ra^*_{crit}	Re	Re_{pol}	$E^{\ell=1}_{tor}/E_k$	Nu	Var_{pol}	N_r	ℓ_{max}	m_s
			$E = 3 \times 10^{-4}$					
1.61	3.4	0.39	0.39	1.058	0	49	48	1
3.22	5.8	0.64	0.64	1.124	0	33	53	1
5.36	41.0	12.6	0.66	1.342	0.25	33	53	1
6.70	60.9	15.3	0.743	1.454	0.34	33	53	1
8.04	80.6	19.6	0.802	1.564	0.45	33	53	1
11.5	136.0	31.1	0.845	2.04	0.33	33	53	1
16.1	205.0	51.1	0.837	2.95	0.15	41	66	1
21.4	273.0	75.8	0.812	4.09	0.14	41	66	1
37.5	407.0	136.0	0.746	6.52	0.08	41	80	1
53.4	490.0	183.0	0.68	8.37	0.07	41	80	1
80.4	580.0	253.0	0.57	10.7	0.06	49	106	1
107.0	633.0	323.0	0.42	12.6	0.06	49	106	1
			$E = 10^{-4}$					
1.15	4.9	2.3	0.18	1.020	0	33	42	2
1.54	9.7	3.6	0.47	1.044	0	33	42	2
3.23	27.9	6.8	0.74	1.107	0	33	42	2
3.70	32.6	7.5	0.76	1.120	0.33	33	42	2
4.30	41.1	8.2	0.805	1.123	0.33	33	53	2
5.13	49.6	9.7	0.816	1.152	0.38	33	53	2
6.42	76.4	14.1	0.856	1.255	0.42	41	64	2
8.60	128.0	21.5	0.895	1.41	0.86	41	64	2
11.5	212.0	35.4	0.912	1.74	1.07	41	85	2
16.0	355.0	58.3	0.925	2.52	0.71	41	85	2
23.0	528.0	97.4	0.916	3.83	0.32	41	85	2
30.7	699.0	143.0	0.903	5.45	0.20	41	85	2
50.0	977.0	235.0	0.871	8.55	0.12	49	106	2
77.0	1250.0	340.0	0.840	11.8	0.10	49	106	2
100.0	1420.0	434.0	0.797	15.4	0.07	65	134	2
			$E = 3 \times 10^{-5}$					
1.19	6.1	2.7	0.29	1.015	0	33	53	2
1.49	12.3	4.0	0.57	1.031	0	33	53	2
2.24	25.3	5.6	0.72	1.051	0.23	33	53	2
4.48	75.6	11.7	0.884	1.125	0.57	41	80	2
7.46	173.0	22.8	0.924	1.27	1.02	49	106	2
11.6	423.0	51.8	0.952	1.74	1.56	41	85	2
16.8	725.0	78.7	0.967	2.32	1.12	49	106	2
22.4	1053.0	119.0	0.968	3.24	0.80	49	106	2
33.6	1510.0	204.0	0.956	5.43	0.30	65	133	2
44.8	1920.0	286.0	0.949	7.75	0.23	65	133	2
74.6	2730.0	503.0	0.926	13.7	0.11	81	168	2
101.0	3390.0	656.0	0.914	17.9	0.07	81	168	2
134.0	3740.0	877.0	0.885	24.7	0.07	81	201	2
			$E = 10^{-5}$					
1.49	14.5	4.5	0.62	1.026	0	65	134	16
11.9	762.0	66.0	0.973	1.61	1.90	65	134	2
19.9	1710.0	138.0	0.982	2.61	1.57	65	134	2
29.9	2700.0	222.0	0.983	4.14	0.98	81	168	2
44.8	3850.0	387.0	0.976	7.33	0.40	81	168	2
79.6	6070.0	790.0	0.963	16.6	0.15	81	201	4
105.0	7310.0	1040.0	0.958	22.9	0.08	81	201	4
			$E = 10^{-5}$ rigid					
42.6	1206.0	607.0	0.296	12.9	0.12	81	168	4

TABLE 2. Results for $Pr = 1$.

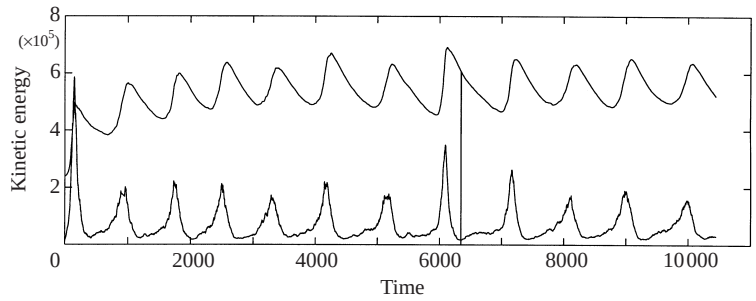

FIGURE 4. Kinetic energy vs. time for $E = 3 \times 10^{-5}$ and $Ra/Ra_{crit} = 22.4$. The upper line is the full energy and the lower line is the poloidal part tenfold enhanced. The vertical line marks the time at which the original restriction to even-order modes is relaxed.

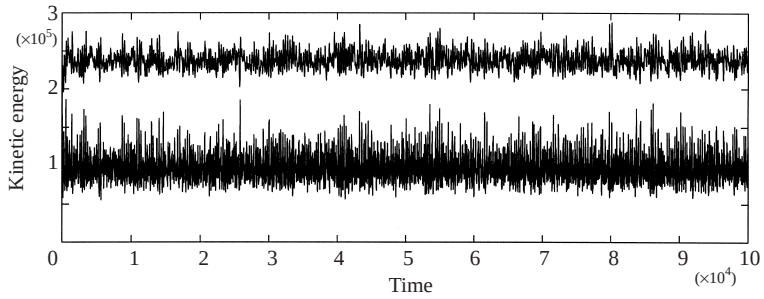

FIGURE 5. Kinetic energy vs. time for $E = 10^{-4}$ and $Ra^*/Ra^*_{crit} = 30.7$, $m_s = 2$. The upper line is the full energy and the lower line is the poloidal part tenfold enhanced.

almost exponential decay of the kinetic energy during periods when convection is inactive. From the example in figure 1(*a*) a decay time of $0.05D^2/\nu$ is derived. Other cases give very similar results. At low and intermediate Rayleigh number each run was followed for at least 0.3 diffusion times (or six relaxation times), some for much longer.

In the regime of fully developed convection the advective transport of momentum (and heat) should control the adjustment time. The inverse of the poloidal Rossby number provides a measure of the time scale of radial advection, i.e. the time needed for a particle to traverse one shell thickness. All runs at $Ra^*/Ra^*_{crit} > 20$ cover at least 25 radial advection times. For the case in figure 1(*c*) a least-squares fit to the total kinetic energy of the form $E(t) = E_\infty - a\exp(-\gamma t)$ has been calculated (excluding times $t < 300$ when the adjustment seems to proceed at a more rapid rate than later). The best-fitting value $\gamma = 6.65 \times 10^{-4}$ corresponds to a relaxation time of $0.016D^2/\nu$. This is faster by a factor of three than the purely viscous relaxation determined above and it suggests that the total run time corresponding to $0.093\,D^2/\nu$ is adequate. The best-fit value of $E_\infty = 2.68 \times 10^7$ differs by less than 1% from the simple average of the energy for $t > 5000$, which has been used to calculate the Reynolds number listed in table 2.

In order to check if very long time scales may be present in the evolution of the solutions, the case of fully developed convection at $E = 10^{-4}$, $Ra^*/Ra^*_{crit} = 31$ was selected to run until $t = 10^5$, i.e. ten diffusion times. This run time is about 50 times longer than what was typically employed at similar parameter values. No long-term variations are seen in the time series of the total and poloidal kinetic energy

(figure 5). The long-term averages differ by no more than 2% from the originally derived values for the interval $t = 570$–2000, suggesting that the solution is past the initial transient at $t > 570$. To estimate the uncertainty which arises from averaging the chaotic fluctuations over a limited time interval, the complete time series has been subdivided into 66 intervals of length 1500 and averages have been calculated for each interval separately. The 2σ standard deviation of the individual averages from the global mean is less than 3% for all properties listed in table 2.

These tests suggest that the results are not seriously affected by the azimuthal symmetry assumption. It may have an effect in certain regimes. For example, the imposed symmetry would suppress a mode termed localized convection by Grote & Busse (2001), who found that active convection was restricted to one azimuthal hemisphere at 3.5 times supercritical Rayleigh number. The tests also suggest that the results are equilibrated, although it cannot be excluded that long time scales may play a role in parameter regimes where such tests are not possible because of computational limitations. The error of the tabulated values, arising from limited integration time, is unlikely to exceed a few percent.

3.3. *Scaling in the limit* $E \to 0$

When represented as function of Ra/Ra_{crit} the characteristic properties of the flow show a strong dependence on the Ekman number (compare figure 1 in Christensen 2001). The asymptotic behaviour in the limit where viscosity (and thermal diffusivity) play a negligible role, i.e. at very low Ekman number and strongly supercritical Rayleigh number, is of particular interest. For investigating whether such asymptotic behaviour can be found in the present results, the conventional Rayleigh number Ra is not very useful. Instead the numerical results are analysed as a function of the modified Rayleigh number Ra^*, which depends on neither diffusion constant. In this case, differences in the viscous force are solely expressed by different values of the Ekman number. Also, substituting the Nusselt number Nu by its modified value Nu^* removes the dependence on thermal diffusivity.

Figure 6 shows various flow properties plotted against Ra^*. In order to emphasize the regime of strong zonal wind, only cases are included in which the zonal flow carries at least 75% of the total energy. The two Rossby numbers in figure 6(a, b) indicate respectively the vigour of the flow in general (dominated by the zonal wind contribution) and that of the convective part alone. There is a change in slope, in particular for Ro, which at high Ra^* increases less with the Rayleigh number than the poloidal Rossby number. The ratio of total kinetic energy to that in the non-zonal part of the flow in figure 6(c), which for values $\gg 1$ is almost the same as the ratio of zonal energy to non-zonal energy, rises with Ra^* at low Rayleigh number. It reaches a maximum value where the flow passes from the oscillatory regime to the fully developed convection regime, but falls with increasing Ra^* in the latter regime. The height of the maximum depends on the Ekman number. The slopes for the modified Nusselt number (figure 6d) flatten out towards low Rayleigh number. This is because in rotating convection the heat flux significantly exceeds the conductive flux only in the fully developed regime when the convective flow fills the entire shell (Tilgner & Busse 1997). In this regime the Nusselt number rises sharply with Ra^*.

For a given value of Ra^* different values of E (shown as different symbols in figure 6) indicate the varying influence of viscous stresses, while everything else remains equal. The four different data sets seem to converge when Ra^* is fixed and the Ekman number is decreased. The convergence is quite obvious for the energy ratios in figure 6(c) on the falling branches of the curves at high Ra^*, but is also

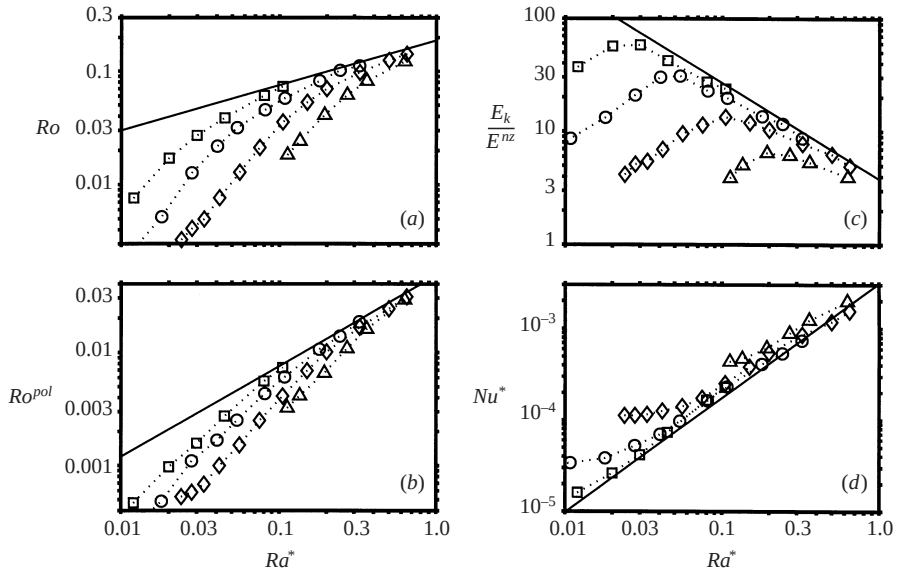

FIGURE 6. Time-averaged properties plotted against modified Rayleigh number for $Pr = 1$. (*a*) Rossby number, (*b*) Rossby number for the poloidal flow component, (*c*) ratio of total kinetic energy to that of the non-zonal flow, (*d*) modified Nusselt number. Triangles are for $E = 3 \times 10^{-4}$, diamonds for $E = 10^{-4}$, circles for $E = 3 \times 10^{-5}$, and squares for $E = 10^{-5}$.

found for the other flow properties. It is best seen for a fixed $Ra^* \approx 0.1$, where data for all four values of E are available. In fact, at $Ra^* = 0.1$ an asymptotic limit seems to be almost reached at the lowest value of $E = 10^{-5}$, i.e. in this case viscous friction plays a small role. The asymptotic limit is approached more rapidly, i.e. already at larger Ekman number, for high values of Ra^*.

Possible asymptotes for the limit $E \to 0$ are drawn as solid lines in figure 6. They have been estimated by eye, using the results at the highest values of the Rayleigh number to align the slopes. The following asymptotic dependences are suggested:

$$Ro = 0.19(Ra^*)^{2/5}, \tag{3.1}$$

$$Ro^{pol} = 0.048(Ra^*)^{4/5}, \tag{3.2}$$

$$E_k/E^{nz} = 3.8(Ra^*)^{-0.85}, \tag{3.3}$$

$$Nu^* = 0.0031(Ra^*)^{5/4}. \tag{3.4}$$

In figure 7 the same results are plotted against the flux-based Rayleigh number $Ra_q^* = Ra^* Nu^*$. Overall the figure is very similar, but the slopes have changed. In this case the slope for the poloidal Rossby has been taken from a scaling analysis (see § 3.4):

$$Ro = 0.65(Ra_q^*)^{1/5}, \tag{3.5}$$

$$Ro^{pol} = 0.54(Ra_q^*)^{2/5}, \tag{3.6}$$

$$E_k/E^{nz} = 0.36(Ra_q^*)^{-2/5}, \tag{3.7}$$

$$Nu^* = 0.077(Ra_q^*)^{5/9}. \tag{3.8}$$

How closely the asymptotic limit is approached depends on the degree of super-

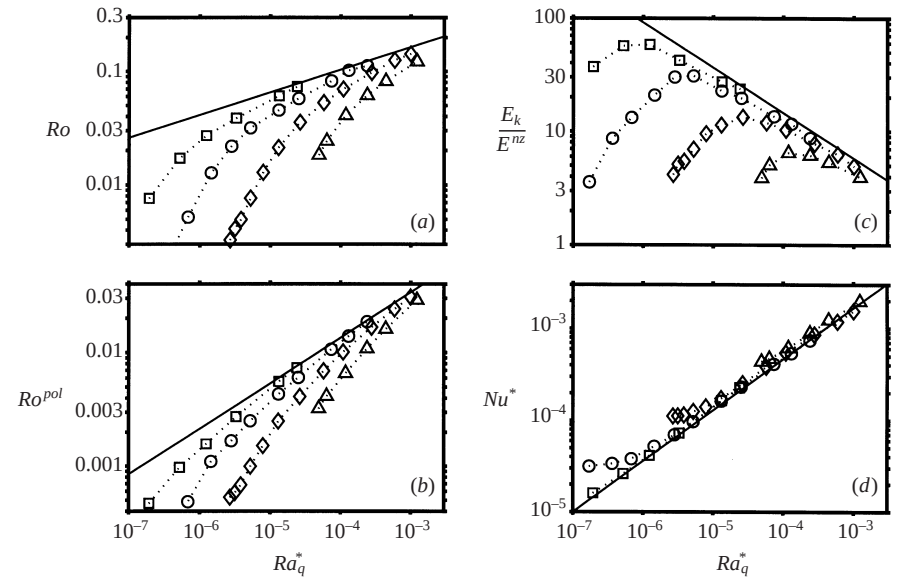

FIGURE 7. Time-averaged properties plotted against modified flux-based Rayleigh number for $Pr = 1$. (*a*) Rossby number, (*b*) Rossby number for the poloidal flow component, (*c*) ratio of total kinetic energy to that of the non-zonal flow, (*d*) modified Nusselt number. Symbols for different Ekman numbers as in figure 6.

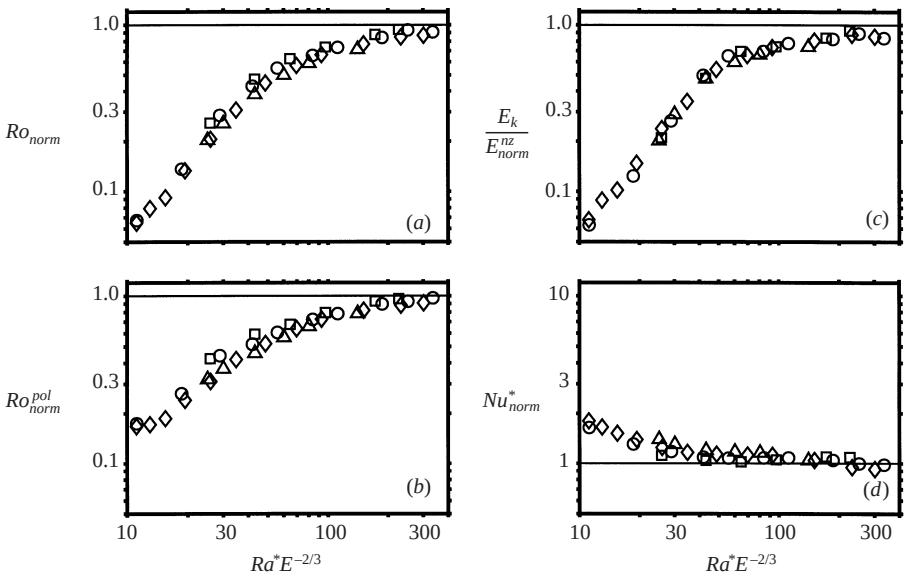

FIGURE 8. Properties as in figure 7 normalized by their asymptotic values and plotted against $Ra^*E^{-2/3}$. (*a*) Rossby number, (*b*) Rossby number for the poloidal flow component, (*c*) ratio of total kinetic energy to that of the non-zonal flow, (*d*) modified Nusselt number. Symbols for different Ekman numbers as in figure 6.

criticality. To quantify the deviation of the four properties, the numerical results have been normalized with the predicted asymptotic values (3.5)–(3.8). A normalized value of 1 means that the numerical result falls exactly on the asymptote. In figure 8 the normalized values are plotted against $Ra^*E^{-2/3}$. In the limit of small Ekman number

this is proportional to the ratio Ra^*/Ra^*_{crit}. Taking the asymptotic form for the critical Rayleigh number was found to give a better fit than plotting the normalized data against the actual ratio Ra^*/Ra^*_{crit}. The points for different Ekman number in the various diagrams in figure 8 are very nearly collapsed on a single curve. This lends further support to the correctness of the asymptotic laws. The asymptotic limit is virtually reached when

$$200E^{2/3} < Ra^*. \tag{3.9}$$

3.4. *Comparison with scaling analysis; Reynolds stresses*

Cardin & Olson (1994) presented a simplified analysis of convection in a rotating sphere based on the 'quasi-geostrophic assumption' of columnar convection cells. At leading order the balance is between the Coriolis force and pressure gradient. Because of the inclination of the boundaries, geostrophy cannot be perfectly satisfied and to next order an equation for the vorticity averaged along the column is derived into which buoyancy forces and the local slope of the boundary at the ends of the column enter. Aubert *et al.* (2001) use this theory for deriving scaling relations for the dependence of the convective velocity and other relevant properties on the fundamental control parameters. They obtain different scaling relations for two limiting cases, where they neglect either the viscous term or the inertia term in their equation. In the limit of negligible viscosity they arrive at a simple 2/5 power dependence between Ra^*_q (called γ in their notation) and the characteristic Rossby number for the convective flow. This dependence has been used for the slope of the asymptote in figure 7(*b*) and is in good agreement with the trend in the numerical results. When viscosity is retained and inertia dropped, the scaling relation given by Aubert *et al.* (2001) is $Ro^{pol} \sim (Ra^*_q)^{1/2}E^{-1/6}$. Earlier, Zhang (1991) had used finite-amplitude calculations at infinite Prandtl number, i.e. without inertial effects, at slightly supercritical Rayleigh number to derive a scaling relation for the convective velocity $u \sim (Ra - Ra_{crit})^{1/2}$ in the limit of low Ekman number. Since $Nu \simeq 1$ at weakly supercritical Rayleigh number there is no significant difference between the flux-based and the temperature-based Rayleigh number and when Zhang's (1991) results are extrapolated to $Ra \gg Ra_{crit}$ the dependence on the Rayleigh number is the same as that derived by Aubert *et al.* (2001) in the viscous limit. The steepening of the slope towards lower Rayleigh number in figure 7(*b*), where at small Reynolds numbers inertia becomes less important in comparison to viscosity, agrees qualitatively with these predictions.

The scaling analysis by Aubert *et al.* (2001) predicts in the 'inertial limit' that the characteristic size of the convective vortices increases weakly with the 1/5 power of the Rayleigh number. I have not attempted here to quantify the vortex size, but an indirect argument for an increase with the Rayleigh number can be advanced. The Nusselt number cannot be predicted from the scaling analysis. The relation between Nu^* and Ra^*_q derived from the numerical results has implications for the characteristic non-dimensional temperature contrasts δT between rising and sinking flow in a vortex. In the limit $Nu \gg 1$ the modified Nusselt number scales as $Nu^* \sim Ro^{pol}\delta T$. Because Nu^* increases more strongly with the Rayleigh number than the convective velocity, δT must increase with Ra^*_q, though weakly. This increase of the temperature fluctuations is more plausible when the size of the convective vortices also increases with the Rayleigh number.

The zonal flow is driven by Reynolds stresses arising from a systematic correlation of the azimuthal component v_ϕ and the cylindrically radial component v_s of the convective flow. Here $v_\phi = u_\phi - U_\phi$ and $v_s = u_s$ are the 'fluctuating' velocity components and U_ϕ is the azimuthal average of u_ϕ, that is, the large-scale zonal flow. Reynolds

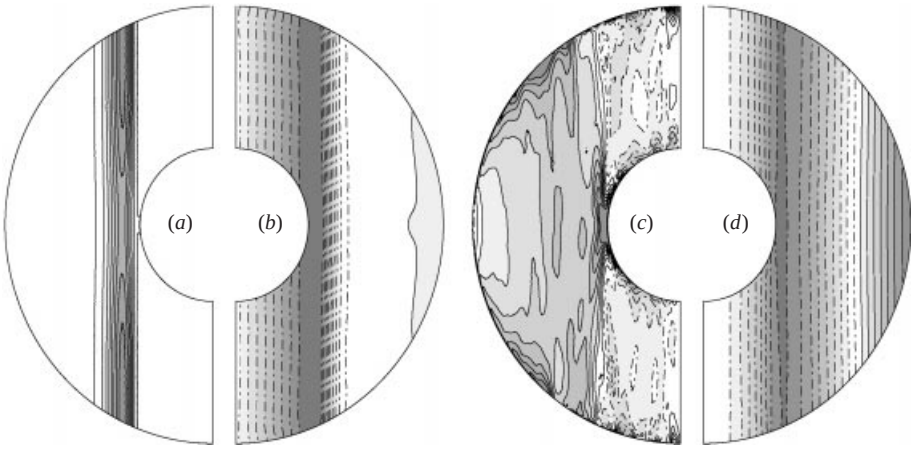

FIGURE 9. Properties averaged in azimuth and time in a cross-section along the rotation axis for (a,b) $Ra^* = 0.0015$ and (c,d) $Ra^* = 0.045$ at $E = 10^{-5}$ and $Pr = 1$, i.e. the cases shown in figures 2 and 3, respectively. (a) and (c) The Reynolds stress $\{\langle v_\phi v_s \rangle\}$ with contour intervals of 3×10^{-9} and 8×10^{-7}, respectively. (b) and (d) U_ϕ with contours of 3×10^{-5} and 8×10^{-3}, respectively. Broken lines for negative contour values; greyscale indicates absolute magnitude.

stresses are usually associated with turbulent boundary layers, where they take energy out of the large-scale flow. Here they feed energy into the zonal flow. For some cases the time-averaged Reynolds stress has been calculated explicitly and is illustrated in figure 9(a,c). The Reynolds stress (more specifically, its ϕs-component) is given by

$$S_R(\theta, r) = \{\langle v_s v_\phi \rangle\} \tag{3.10}$$

where $\langle\ \rangle$ stands for the average taken over ϕ and $\{\ \}$ for the time average. At weakly supercritical Rayleigh number the only significant Reynolds stresses are positive and are nearly uniform along the z-direction inside the convection columns (figure 9a). They transport angular momentum in the radially outward direction, which explains the variation of U_ϕ with s (figure 9b).

The scaling analysis by Aubert *et al.* (2001) for the zonal flow velocity is not applicable here because they assumed rigid boundaries. In that case the zonal flow is limited by Ekman layer friction, whereas with free boundaries the Reynolds stresses are balanced by the weaker viscous stress

$$S_V = Es\partial \left(\frac{U_\phi}{s} \right) \Big/ \partial s \tag{3.11}$$

due to internal friction. When estimating the Reynolds stresses, Aubert *et al.* (2001) assumed that the degree of correlation between v_s and v_ϕ is independent of the Rayleigh number, in which case the Reynolds stress increases proportionally to $(Re^{pol})^2$. Because the length scale on which U_ϕ varies is of order one, balancing the stresses in equations (3.10) and (3.11) gives

$$Re^{zon} \sim (Re^{pol})^2 \tag{3.12}$$

where Re^{zon} is the Reynolds number of the zonal flow component alone. The quadratic relation is confirmed for weakly supercritical conditions (figure 10), but breaks down for convective Reynolds numbers $Re^{pol} > 10$. This causes the slopes in the diagrams for the kinetic energy ratio in figures 6(c) and 7(c) to bend over and eventually to become negative.

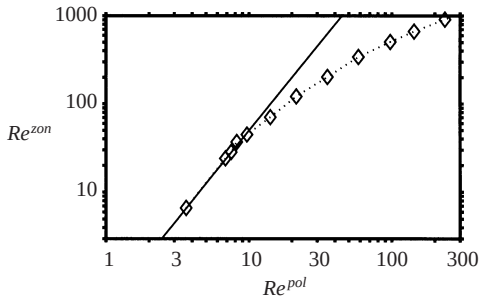

FIGURE 10. Reynolds number of the mean zonal flow versus Reynolds number of the convective flow for $E = 10^{-4}$. The solid line has a slope of 2.

Ra^*/Ra^*_{crit}	1.49	11.9	44.8	42.8	105.0
b.c.	F	F	F	R	F
C_R^{out}	0.831	0.392	0.185	0.150	0.051
C_R^{in}	0.008	0.074	−0.055	0.017	−0.030

TABLE 3. Correlations at $E = 10^{-5}$; boundary condition *b.c.* F = free, R = rigid.

The deviation from the quadratic dependence is caused by a decorrelation of the fluctuating velocity components with increasing Rayleigh number. In some cases the correlation coefficient

$$C_R = \frac{\{[\langle v_s v_\phi \rangle]\}}{\left\{\left[\sqrt{\langle v_s^2 \rangle \langle v_\phi^2 \rangle}\right]\right\}} \tag{3.13}$$

has been calculated, where [ ] indicates the average taken over z and s. The correlation has been calculated separately for the regions inside and outside the tangent cylinder and is listed in table 3, labelled C_R^{in} and C_R^{out}, respectively. Outside the tangent cylinder it decreases from near-perfect correlation at low Rayleigh number to very weak but still positive correlation at high Rayleigh number.

There seem to be two possible causes for the decorrelation. The preferred tilt of the convection columns could decrease when inertial and/or buoyancy effects play an increasingly important role in the force balance at high Rayleigh number. Alternatively, the mean zonal flow may develop shear-flow instabilities, which create Reynolds stresses of the opposite sign compared to the Reynolds stresses of columnar convection and largely cancel them. In order to discriminate between these two possible explanations, one calculation has been done with rigid boundaries at $E = 10^{-5}$. Compared with the free-slip case at the same Rayleigh number, about 45 times critical (table 2), the convection is somewhat stronger and Reynolds stresses are of similar order, but the zonal flow is much weaker with a Reynolds number of $Re^{zon} = 650$ compared to 3800 in the free-slip case. The very similar degree of correlation of the fluctuating velocity components (table 3) suggests that shear-flow instabilities are not dominant in weakening the driving Reynolds stresses.

A plausible cause for the decorrelation is the gradual loss of geostrophy of the convection columns at high Rayleigh number, which we note for example in figure 3(*c*) where the vortices are no longer continuous along the entire cord in z. The same disruption of vortices is found also in the case of rigid boundaries (not shown). A

Ra^*/Ra^*_{crit}	Re	Re_{pol}	$E^{\ell=1}_{tor}/E_k$	Nu	Var_{pol}	N_r	ℓ_{max}	m_s
			$Pr = 0.3$					
1.54	18.7	5.7	0.668	1.013	0	33	42	2
4.1	73.8	12.5	0.864	1.040	0.31	41	64	2
8.2	188.0	29.0	0.907	1.136	0.37	41	64	2
12.4	390.0	67.0	0.910	1.39	0.38	41	64	2
16.5	628.0	133.0	0.882	1.98	0.21	41	85	2
24.7	980.0	261.0	0.832	3.44	0.14	41	85	2
41.2	1370.0	428.0	0.780	5.43	0.09	49	106	2
49.5	1530.0	518.0	0.738	6.62	0.08	65	134	2
			$Pr = 3$					
1.54	4.6	2.0	0.206	1.088	0	33	42	2
8.1	58.0	15.1	0.748	2.15	0.28	41	64	2
16.2	170.0	32.5	0.889	3.91	0.34	41	85	2
32.5	363.0	62.3	0.927	6.79	0.24	49	106	2
48.8	510.0	92.4	0.924	9.65	0.18	65	134	2
65.0	640.0	120.0	0.921	12.3	0.13	65	134	2
108.0	893.0	187.0	0.906	17.8	0.09	65	134	2

TABLE 4. Results for different Prandtl numbers at $E = 10^{-4}$.

prime cause for the prograde tilt of the convection columns is the convex curvature of the outer boundary on which the columns impinge (Busse 1983, 1994). Obviously, it requires nearly perfect geostrophy to maintain the tilt along the entire length in z of the column. When geostrophy is broken, a vortex near the equatorial plane does not 'feel' the curvature of the boundary. This idea is supported by the spatial distribution of the Reynolds stresses in figure 9(c), which are strongest close to the boundaries. Although part of the reason is that the convective velocities are somewhat larger in these regions, the degree of correlation is also found to be higher where the vortices still 'feel' the influence of boundary curvature.

3.5. *Effect of Prandtl number*

The numerical work by Zhang (1992) and the experimental results by Aubert *et al.* (2001) strongly suggested that the value of the Prandtl number plays an important role in the presence of a strong zonal flow. They observed a dominant zonal wind only for moderately low Prandtl number $Pr \leqslant 1$. Here I have studied the influence of the Prandtl number within the limited range $Pr = 0.3$–3 for an Ekman number of 10^{-4}. Results are listed in table 4 and can be compared with the data in table 2 for the same value of the Ekman number.

At weakly supercritical Rayleigh number the strong dependence of the zonal wind on the Prandtl number is confirmed. At $Ra^*/Ra^*_{crit} = 1.54$ the contribution of the mean zonal flow to the total kinetic energy decreases with the Prandtl number from 67% at $Pr = 0.3$ to 21% at $Pr = 3$. However, this strong dependence does not persist at higher Rayleigh numbers. When the Reynolds number becomes sufficiently large so that strong Reynolds stresses can develop, a very dominant zonal flow is also obtained for $Pr > 1$. The maximum fraction of kinetic energy in the wind flow (at the optimum Rayleigh number) is nearly independent of the Prandtl number.

One might hope that in the limit $E \to 0$ the dependence on the Prandtl number vanishes and the properties of convection and zonal flow depend on Ra^* or Ra^*_q alone.

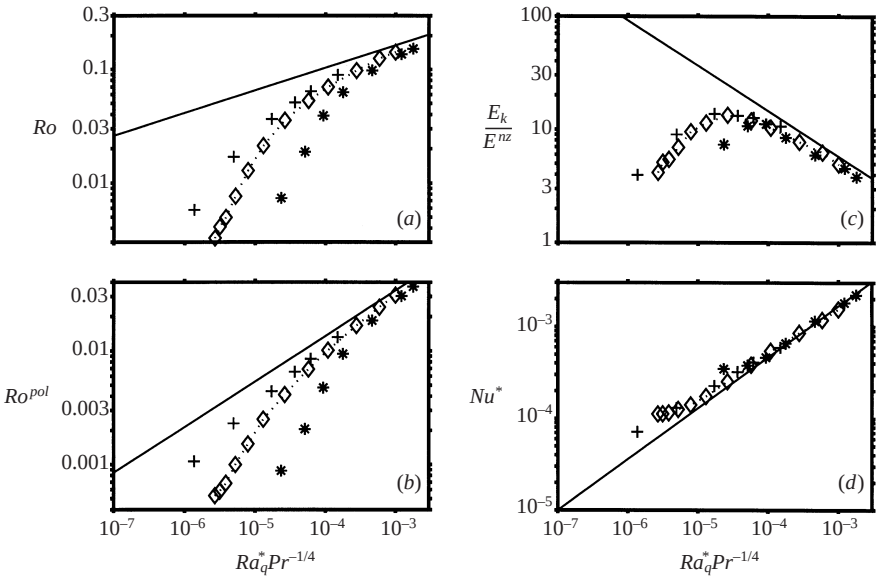

FIGURE 11. Time-averaged properties plotted for different Prandtl number at $E = 10^{-4}$. (*a*) Rossby number, (*b*) Rossby number for the poloidal flow component, (*c*) ratio of total kinetic energy to that of the non-zonal flow, (*d*) modified Nusselt number. Diamonds are for $Pr = 1$, crosses for $Pr = 0.3$ and stars for $Pr = 3$. The asymptotic lines are those given by equations (3.5)–(3.8), but with Ra_q^* replaced by $Ra_q^* Pr^{-1/4}$.

But plotting the available data against these Rayleigh numbers (not shown) suggests a weak dependence on Pr in the asymptotic limit also. The data for different Pr at $E = 10^{-4}$ can be collapsed at high Rayleigh number when plotted against $Ra_q^* Pr^{\alpha}$, where the exponent α is in the range of $-1/4$ to $-1/3$ (figure 11).

4. Discussion

Although the Ekman numbers used in this study are large in comparison with planetary values, the convergence of the results with decreasing Ekman number suggests that a regime is approached where viscosity becomes unimportant. This limit seems to be almost reached in some of the calculations, which provides a justification for scaling the numerical results to the planets as done by Christensen (2001) and Aurnou & Olson (2001). These authors suggested that zonal flow velocities in agreement with observed values on Jupiter and Saturn can be obtained by the deep convection mechanism. The asymptotic dependences on the modified Rayleigh numbers, which are derived from the numerical results, are somewhat uncertain. The residual deviations from the asymptotes are not negligible and prevent a more rigorous determination of the exponents, which must be considered as quite tentative. For an application to the planets this is not too critical, because the numerical calculations cover the likely values of the modified Rayleigh number in Jupiter or Saturn (see below) and no extrapolation outside the range is necessary.

Because the driving superadiabatic temperature contrast is unknown for convection in the Earth's core or in the gas planets, but observations or estimates are available for the heat flow, the scaling laws based on the Rayleigh number defined with the heat flux should be particularly useful. The relevance of the present results is limited in the case of the Earth's core because of the influence of the magnetic field and in the

case of the gas planets because of compressibility effects. Nonetheless it is interesting to consider what the scaling laws predict for the two systems.

Estimates for the superadiabatic heat flux out of the Earth's core are of the order $10\,\mathrm{mW\,m^{-2}}$ (Buffett *et al.* 1996), which translates into a value for the Rayleigh number of $Ra_q^* \simeq 10^{-13}$. The corresponding value of Ra^* is 2×10^{-6} from (3.8) and the condition (3.9) is met well for an Ekman number of 10^{-15}. The scaling relations predict a Rossby number for the convective flow of about 3×10^{-6}, corresponding to a velocity of $0.5\,\mathrm{mm\,s^{-1}}$, which is the order of magnitude estimated from secular variations of the Earth's magnetic field (Bloxham & Jackson 1991). The predicted zonal flow is too large by three orders of magnitude. The strong damping of zonal flow is not primarily due to friction in the Ekman layer at the boundary towards the solid mantle, but is mainly caused by electromagnetic Maxwell stresses in the conducting core which strongly couple the differentially rotating cylinders.

Compressibility is important in the molecular hydrogen envelopes of the major planets, which extend over many density scale heights. Here lies the main difficulty in applying the present results, obtained for a Boussinesq fluid, directly to these planets. For a compressible fluid in the geostrophic limit the Proudman–Taylor theorem holds for the mass flux $\rho \boldsymbol{u}$ in place of the velocity $\boldsymbol{u}$. Hence both the velocity of columnar convection and that of the zonal flow would be expected to decrease with depth in the planets. A reasonable approach for utilizing the Boussinesq results could be to use the physical properties at the surface of the planets (by definition the 1 bar pressure level), where the flow velocities are known from observations. Taking Jupiter's observed excess heat flux of $6\,\mathrm{Wm^{-2}}$ and $D \simeq 10^4\,\mathrm{km}$ ($\eta \simeq 0.85$), $\alpha = 1/T \simeq 10^{-2}\,\mathrm{K^{-1}}$, $\rho \simeq 0.2\,\mathrm{kg\,m^{-3}}$, $g_o \simeq 25\,\mathrm{m\,s^{-2}}$, $\Omega \simeq 1.75 \times 10^{-4}\,\mathrm{s^{-1}}$, $c \simeq 14\,\mathrm{kJ\,kg^{-1}\,K^{-1}}$, the flux-based Rayleigh number is $Ra_q^* \simeq 10^{-6}$. For this Rayleigh number the scaling relations predict a Rossby number of 0.04 and a ratio of 1:90 between the non-zonal and the total kinetic energy. The corresponding velocity of $70\,\mathrm{m\,s^{-1}}$ agrees very reasonably with the observed mean flow velocity at low and mid-latitudes on Jupiter. The ratio of zonal to non-zonal kinetic energy is also correct on an order-of-magnitude basis, but slightly on the high side (Ingersoll *et al.* 1981). However, it remains unclear if the vortices at the planetary surfaces representing the non-zonal flow are associated with deep-reaching convection or are instabilities in a shallow atmospheric layer.

At the surfaces of Jupiter and Saturn a substantial number of bands with alternating flow directions is observed, whereas in the present convection models only a change from prograde flow near the equator to retrograde flow at high latitude is found. Models with a larger core radius $\eta = 0.6$ (Christensen 2001) exhibited additional bands of zonal flow with alternating directions inside the tangent cylinder. However, comparing models for the internal structure of the giant planets (e.g. Guillot 1999) with the observed zonal wind pattern suggests that multiple bands must exist also outside the tangent cylinder. Busse (1983, 1994) envisioned that at high Rayleigh number stacked layers of convection columns would occur and that between these layers the mean zonal flow would change direction. In the present high-Rayleigh-number calculations multiple convective vortices exist in the radial direction (figure 3*b*), though not in well-defined layers. However, they all create Reynolds stresses of positive sign outside the tangent cylinder and therefore they do not give rise to multiple zonal flow bands. In fact, when convex or concave boundary curvature determines the sign of the Reynolds stresses, it is not clear how alternating bands can be generated. Explaining the number and spacing of bands at the surfaces of the gas planets remains an outstanding problem for the deep convection model.

REFERENCES

Ardes, M., Busse, F. H. & Wicht, J. 1997 Thermal convection in rotating spherical shells. *Phys. Earth Planet. Inter.* **99**, 55–67.

Aubert, J., Brito, D., Nataf, H.-C., Cardin, P. & Masson, J.-P. 2001 A systematic experimental study of rapidly rotating spherical convection in water and liquid gallium. *Phys. Earth Planet. Inter.* **128**, 51–74.

Aurnou, J. M. & Olson, P. L. 2001 Strong zonal winds from thermal convection in a rotating spherical shell. *Geophys. Res. Lett.* **28**, 2557–2560.

Bloxham, J. & Jackson, A. 1991 Fluid flow at the surface of the Earth's outer core. *Rev. Geophys.* **29**, 97–120.

Buffett, B. A., Huppert, H. E., Lister, J. R. & Woods, A. W. 1996 On the thermal evolution of the Earth's core. *J. Geophys. Res.* **101**, 7989–8006.

Busse, F. H. 1970 Thermal instabilities in rapidly rotating systems. *J. Fluid Mech.* **44**, 441–460.

Busse, F. H. 1983 A model of mean zonal flows in the major planets. *Geophys. Astrophys. Fluid Dyn.* **23**, 153–174.

Busse, F. H. 1994 Convection driven zonal flows and vortices in the major planets. *Chaos* **4**, 123–134.

Busse, F. H. & Carrigan, C. R. 1976 Laboratory simulation of thermal convection in rotating planets and stars. *Science* **191**, 81–83.

Cardin, P. & Olson, P. L. 1994 Chaotic thermal convection in a rapidly rotating spherical shell: consequences for flow in the outer core. *Phys. Earth Planet. Inter.* **82**, 235–259.

Christensen, U. R. 2001 Zonal flow driven by deep convection in the major planets. *Geophys. Res. Lett.* **28**, 2553–2556.

Glatzmaier, G. A. 1984 Numerical simulation of Stellar convective dynamos. I. The model and method. *J. Comput. Phys.* **55**, 461–484.

Grote, E. & Busse, F. H. 2001 Dynamics of convection and dynamos in a rotating sphere. *Fluid Dyn. Res.* **28**, 349–368.

Grote, E., Busse, F. H. & Tilgner, A. 2000 Regular and chaotic spherical shell dynamos. *Phys. Earth Planet. Inter.* **117**, 259–272.

Guillot, T. 1999 A comparison of the interiors of Jupiter and Saturn. *Planet. Space Sci.* **47**, 1183–1200.

Ingersoll, A. P., Beebe, R. F., Mitchell, J. L., Garneau, G. W., Yagi, G. M. & Müller, J. P. 1981 Interaction of eddies and mean zonal flow on Jupiter as inferred from Voyager 1 and 2 images. *J. Geophys. Res.* **86**, 8733–8743.

Jones, C. A., Soward, A. M. & Mussa, A. I. 2000 The onset of convection in a rapidly rotating sphere. *J. Fluid Dyn.* **405**, 157–179.

Roberts, P. H. 1968 On the thermal instability for a self-gravitating fluid sphere containing heat sources. *Phil. Trans. R. Soc. Lond.* A **263**, 93–117.

Sumita, I. & Olson, P. L. 2000 Laboratory experiments on high Rayleigh number thermal convection in a rapidly rotating hemispherical shell. *Phys. Earth Planet. Inter.* **117**, 153–170.

Sun, Z.-P., Schubert, G. & Glatzmaier, G. A. 1993 Banded surface flow maintained by convection in a model of the rapidly rotating giant planets. *Science* **260**, 661–664.

Tilgner, A. 1999 Spectral methods for the simulation of incompressible flow in spherical shells. *Intl J. Numer. Meth. Fluids* **30**, 713–724.

Tilgner, A. & Busse, F. H. 1997 Finite amplitude convection in rotating spherical fluid shells. *J. Fluid Mech.* **332**, 359–376.

Williams, G. P. 1985 Jovian and comparative atmospheric modeling. *Adv. Geophys.* **28A**, 381–449.

Zhang, K. 1991 Convection in a rapidly rotating spherical shell at infinite Prandtl number: steadily drifting rolls. *Phys. Earth Planet. Inter.* **68**, 156–169.

Zhang, K. 1992 Spiralling columnar convection in rapidly rotating spherical shells. *J. Fluid Mech.* **236**, 535–556.